THIS DOCUMENT IS PART OF A NEW BOOK, IT IS BROUGHT TO YOU FREELY BY THE OPEN ACCESS JOURNAL MATERIALS AND DEVICES

Publication date: 2021, january 14th

The book,
"PEROVSKITES AND OTHER FRAMEWORK STRUCTURE MATERIALS
(2D-perovskites, Aurivillius, Ruddlesden-Popper, Dion-Jacobson phases, tungsten bronzes, clays, and others)

New trends and perspectives"

(editors P. Saint-Grégoire and M.B Smirnov)

Is a collective volume of 800 pages with **76 authors** and **26 chapters** on recent developments and hot subjects, divided into two parts:

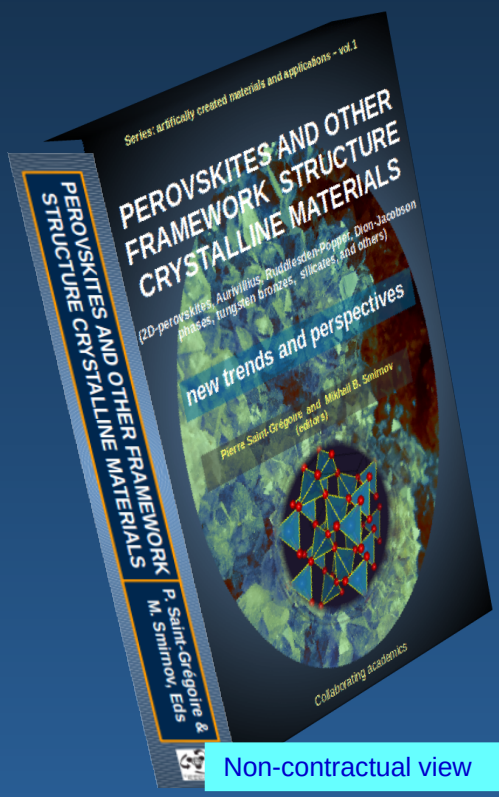

Non-contractual view

A. Fundamental aspects and general properties

B. Elaborated materials and applied properties

Available in 3 formats:

- **Ebook**
- **printed softcover, black & white**
- **printed hardcover, color.**

Go to the Book(click)

Chap. 3 : The intricate lattice dynamics of perovskite oxides

Annette Bussmann-Holder[1], Jae-Hyeon Ko[2], Krystian Roleder[3]

[1] Max-Planck-Institut für Festkörperforschung, Heisenbergstr. 1, D-70569 Stuttgart, Germany

[2] Department of Physics, Hallym University, 1 Hallymdaehakgil, Chuncheon, Gangwondo 24252, Korea

[3] Institute of Physics, University of Silesia, ul. 75 Pułku Piechoty 1, 41-500 Chorzów, Poland

Corresponding author : a.bussmann-holder@web.de

Abstract : The lattice dynamics of perovskite oxides are investigated theoretically within the polarizability model which is a nonlinear approach taking into account anharmonic electron-lattice interactions. The emphasis is on local lattice anomalies which appear in the phonon modes dispersion. Above the actual phase transition temperature finite size polarized clusters appear at an onset temperature T_{BH} which marks the precursor formation temperature. These local anomalies appear as well experimentally and are reviewed for various perovskite compounds.

Keywords: FERROELECTRICS, ANTIFERROELECTRICS, PEROVSKITE OXIDES, PHASE TRANSITIONS, LATTICE and PRECURSOR DYNAMICS

Cite this paper: A. Bussmann-Holder, J-H. Ko, K. Roleder, OAJ materials and Devices, vol 5(1) chap No3 in “Perovskites and other Framework Structure Crystalline Materials”, p103 (Coll. Acad. 2021) DOI:10.23647/ca.md20202805

I. Introduction

Perovskite oxides ABO_3 have attracted immense interest since the discovery of barium titanate $BaTiO_3$ in the 1940th followed shortly afterwards by $SrTiO_3$, $PbTiO_3$, etc. [1]. The reasons for the increased activity in this field are related to the fact that they were the first ferroelectric materials without hydrogen bonds and rapidly replaced those technologically as ultrasound transducers. Opposite to ferroelectrics with hydrogen bonds, as KH_2PO_4, and analogues their phase stability is much better and their use as ceramics for applications much larger. The ability of this material class to tune the temperature range of the polar state and the related properties by doping opened completely new technologically relevant areas which until now have not been superseded by novel material classes. From a theoretical point of view, the standpoint of ferroelectrics as order/disorder phase change materials had to be abandoned with the early discovery of the soft mode driven transition, classified as displacive. This was opposed to the order/disorder mechanism and a rather rigid picture evolved , where a classification into either displacive or order/disorder phase transition mechanism was adopted concluding that both phenomena were mutually exclusive. The intense investigations of ABO_3 systems have established controversies from an experimental point of view since in many of these compounds a distinct difference in local as opposed to global properties were discovered. While spatially local order testing tools, like NMR, EPR and EXAFS, to mention a few, arrived at the conclusion that order / disorder dynamics are relevant to perovskites as well, the long-wave length testing experiments like Raman scattering, x-ray scattering, infrared measurements were interpreted within a purely displacive scenario. Early on, Müller et al suggested [2] that different time and length scales are involved in the respective experiments, thereby resolving the controversies and emphasizing their complementary character. However, even nowadays, there are opposing communities who deny those aspects.

An interesting discovery contributing to the open discussion was made by Burns and Dacol [3], who showed that a new temperature scale is given by the temperature T_d where a ferroelectric material, previously in the paraelectric state, starts developing randomly polarized precursor regions that have been named polar nanoregions (PNR). The original discovery was reported on pure lead titanate ($PbTiO_3$), potassium niobate ($KNbO_3$), and extended to more complex lead lanthanum zirconate titanate (PLZT), lead magnesium niobate (PMN), lead zinc niobate (PZN), $K_2Sr_4(NbO_3)_{10}$, and strontium barium niobate (SBN) and $Na_{1/2}Bi_{1/2}O_3$(NBT) to mention but a few. Meanwhile, many more perovskites and related compounds have been shown to possess PNRs. In this context it is important to introduce relaxor ferroelectrics where PNRs play a decisive role since they have been claimed to be responsible for the frequency dispersion of

the dielectric response. They are technologically of uttermost importance since they find application in high efficiency energy storage and conversion, as they have a large permittivity, orders-of-magnitude higher than those of conventional ferroelectric materials. Relaxor ferroelectrics show permanent dipole moment in their PNRs. Because they are on the nano-length scale, it takes less energy to align them. Consequently, relaxor ferroelectrics have very high specific capacitance and thus have generated interest in the fields of energy storage. Furthermore, due to their slim hysteresis curve with high saturated polarization, low remnant polarization and extraordinary electromechanical properties relaxor ferroelectrics have high discharge energy density and high discharge rates [4]. A full understanding of this class of ferroelectrics is absent in spite of numerous attempts and sophisticated experimental techniques. It is, however, important to mention that relaxor behavior is typically observed in mixed perovskites where the individual components might well show displacive or order/disorder properties.

In the following we address a novel aspect of the phase transitions in ABO_3 perovskites by concentrating on the transition temperature T_C and the preceding temperature regions which exhibit not purely paraelectric behavior but show dynamics prior to the actual transition in terms of precursors which are spatially confined.

II. Polarizability effects in perovskites

Early attempts to understand the complex features of ABO_3 were based on lattice dynamical models since the firstly observed soft mode behavior suggested a strong involvement of the dynamics in the phase transition mechanism quite opposite to hydrogen-bonded compounds where pseudo-spin models were assumed to be sufficient [1]. In these models the ionic character of ABO_3 was modelled by rigid ion models with local double-well potentials in order to account for the polar character in the low temperature phase [5]. In spite of the fact that these approaches were predictive and successful for the understanding of the soft modes, only the overall qualitative behavior could be reproduced whereas any quantitative agreement with experiments remained absent. The possibility to reverse the polar state has been taken as evidence that also for ABO_3 systems a pseudo-spin ansatz could be realizable. Especially for $BaTiO_3$ with its rather large open volume regarding the TiO_3-moiety, off-centering of the Ti ion in the paraelectric phase was observed by NMR and interpreted in terms of an eight-site spin model reflecting order/disorder dynamics opposed to the observed soft modes [6].

Besides of lattice dynamical models and pseudo-spin approaches, electronic structure

calculations were carried out which uniquely arrived at the conclusion that the band structure consists of a predominantly oxygen p derived valence band and a transition metal dominated d-band with an energy gap of several eV, this being dependent on the individual compound. An additional complexity was observed in the lead derived perovskites where the lone pairs of lead contribute to the valence band. In gap states can be activated in oxygen deficient samples or through doping with aliovalent ions, thereby inducing an insulator – metal transition which is still under intense research.

With the advance of density functional theory (DFT) and *ab initio* approaches [7 – 10] the theoretical description became more sophisticated and admitted predictions of novel ground states and phase transition sequences. However, a common failure of these theories lies in the fact that the calculated transition temperatures are away from those observed experimentally and, also, that either the predicted unit cell volume is too large for the realistic structure or the crystalline symmetry is different from the experimental one. Including correlation effects by introducing a Hubbard U term, i.e. a strong onsite Coulomb interaction, which is rather meaningless in these systems since these are ionic insulators, these problems can be overcome at the expense of this extra parameter.

A common feature to all above described approaches is the fact that they rely on an underlying periodic lattice network, thus overlooking or missing features related to local effects relevant at the nano-scale. These are at the heart of the ideas developed below and it will be shown to be compatible with long wave length properties thereby solving long standing controversies.

The model we use is the polarizability model introduced by Migoni, Bilz, and Bäuerle [11]. It is an extension of the shell model of Cowley [12], where the oxygen ion surrounding shell is anisotropically coupled to A and B neighbors, and the coupling with the transition metal d-shell includes, besides of an attractive harmonic term, a repulsive anharmonic nonlinear term. Through the latter, temperature dependent properties are accounted for within the self-consistent phonon approximation (SPA). While also this model, as long as the SPA is used, relies on lattice periodicity, exact solutions of the nonlinear problem exist, which refer to spatially confined solutions in terms of breathers, intrinsically localized modes (ILM), periodons, solitary type solutions, kinks, and nonlinear travelling wave excitations [13]. By superposing lattice and nonlinear solutions, a novel dynamical pattern is discovered where momentum dependent anomalies suggest spatial anomalies in the lattice displacement pattern [14]. An example of the latter case is shown in Figures 1, where the upper figure refers to a breather solution whereas in the lower one the superposition is depicted which consists of three areas, namely the pure wave regime, the breather region and an

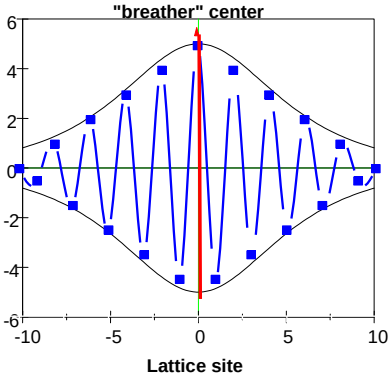

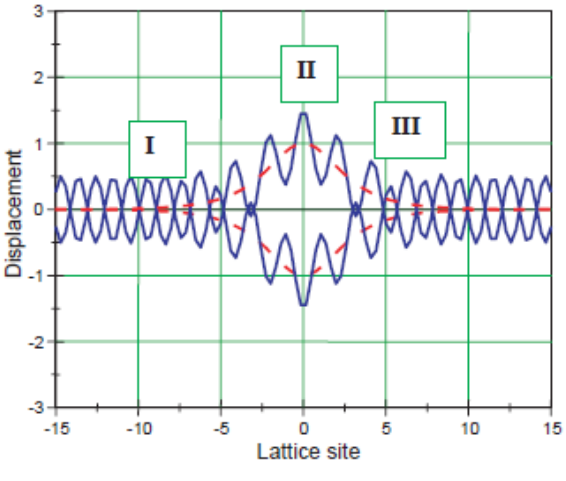

Figure 1 (upper) Displacement of ion 1 with mass M_1 within the breather region (blue lines). The breather center is marked by the red line. The black lines correspond to an envelope function proportional to l 1/cosh l

Figure 1 (lower) Superposition of the regular lattice (I) and breather displacements (II). Region III is the regime where interactions between I and II are relevant. The red dashed line corresponds to an averaged envelope function [after 14].

interstitial area, where the lattice solution transforms into the breather. These ILM solutions are relevant for relaxor ferroelectrics since they bear a close resemblance with PNR's.Another option to detect anomalies in the dynamics is to investigate closer the dispersion of the relevant lattice modes with emphasis on the regions where mode-mode coupling occurs. This is especially important in those systems which exhibit pronounced mode softening, since the energy lowering of a specific phonon mode is not confined to a single momentum value but relates to an extended momentum space where other modes come into play. This point has been addressed early on, in view of the observation of anomalies in the acoustic mode dispersion of various ferroelectrics, and has been modelled by introducing *ad hoc* couplings between the soft mode and the related transverse acoustic mode [15, 16]. However, little attention was devoted to it subsequently.

Within the polarizability model, a temperature and momentum dependent coupling term has been derived self-consistently, which quantitatively reproduces the observed anomalies [17]. This anomalous acoustic mode softening can be related to an inherent lattice instability at finite momentum that covers a limited momentum region corresponding to spatially limited dynamically displaced regions. This issue is addressed in the following by showing that their existence conforms with local anomalies, as observed by local probe testing tools like NMR, EXAFS, PDF. On the other hand the long wave length features relevant to ferroelectrics are simultaneously captured through either q=0 or q=2π/a mode softening.

Various systems are discussed in the following where either the A-site in ABO_3 is varied and B being the same for all compounds, or vice versa, the B-site is replaced by a homologous ion and the A-site remaining the same. The first series are the rare earth titanates, namely, $CaTiO_3$ (CTO), $SrTiO_3$ (STO), $BaTiO_3$ (BTO). These three compounds are rather alike with respect to the A-site which is a rigid ion with valency +2. Their band structures closely resemble each other with even the band gaps being all around 3.5 eV. Their phase transitions are very different from each other in spite of the fact that all three are cubic at high temperature [18]. While CTO undergoes a series of structural transitions and exhibits mode softening although without becoming ferroelectric, STO shows only a single transition from cubic to tetragonal and the related softening of a transverse optic mode. While in STO this mode extrapolates to zero around +28K, for CTO it lays far in the negative temperature range and the naming as quantum paraelectric is hard to justify since quantum fluctuations are not the origin of the suppression of polar order. BTO shows various phase transitions all related to ferroelectric phases with the polarization being rotated to another symmetry direction for the different phases. Its first transition from cubic to tetragonal initiated controversies about its nature since Hyper Raman data evidenced a displacive character whereas NMR results are in support of an order/disorder transition.

The second series is $PbTiO_3$ (PTO), $PbZrO_3$ (PZO), $PbHfO_3$ (PHO) [19]. While the former two are well investigated, much less research activity has been undertaken in PHO. It is, however, well established that PHO undergoes two successive phase transitions at 480 and 440 K, both being antiferroelectric. On the contrary, PZO undergoes a single phase transition to an antiferroelectric phase at about 500 K, which is followed by a transient ferroelectric phase covering approximately 20 K below the transition temperature. This observation is, however, sample and preparation dependent and, in addition, a function of the velocity of the experiment. PTO also exhibits a single transition which takes place at T_C = 763 K and leads to a ferroelectric phase. This transition has long been considered to be a prototypical displacive phase transition displaying strong long wavelength transverse optic mode softening. A revision of this classification has been deduced from by x-ray absorption fine structure (EXAFS) experiments, where tetragonal distortions and Ti and Pb off-centering from the ideal cubic structure have been observed in the paraelectric phase suggesting an order–disorder model. Similar local deviations from the average structure have also been seen in the low-temperature orthorhombic structure of PHO and PZO. The band gap in these three Pb perovskites increases with increasing transition metal mass and follows, thus, related trends observed in analogous series where Pb is replaced by e.g., Ba, Sr, Ca.

For all the above compounds, solutions based on the SPA have been obtained which is a pseudo-harmonic approach and presumes lattice periodicity. In particular the lowest transverse optic (soft) mode and its related transverse acoustic mode are in the focus because these carry the important information on local anomalies. Opposite to former modelling using the SPA, the coupling between both modes induces a temperature dependence in the acoustic zone boundary mode which is less strong as compared to the optic one, but well visible experimentally. The resulting modes for the first series are shown in Figure 2. Interestingly, here optic and acoustic modes cross with decreasing temperature for CTO and BTO, but this is avoided in STO.

While the above results do not provide any information on spatial deviations of the local structure from the average one, a closer inspection of the mode dispersions evidences that in particular the acoustic mode shows anomalies close to the long-wave length limit, which are strongly temperature and momentum dependent and, importantly, start developing already above the actual transition temperature. In a variety of previous work we have identified this temperature regime as a precursor region which is visible in various experiments. In addition, anomalous thermal conductivity has been reported for all investigated compounds and it is shown here to stem from anharmonic phonon-phonon interactions which occur in a limited momentum region, corresponding to a finite size real space regime.

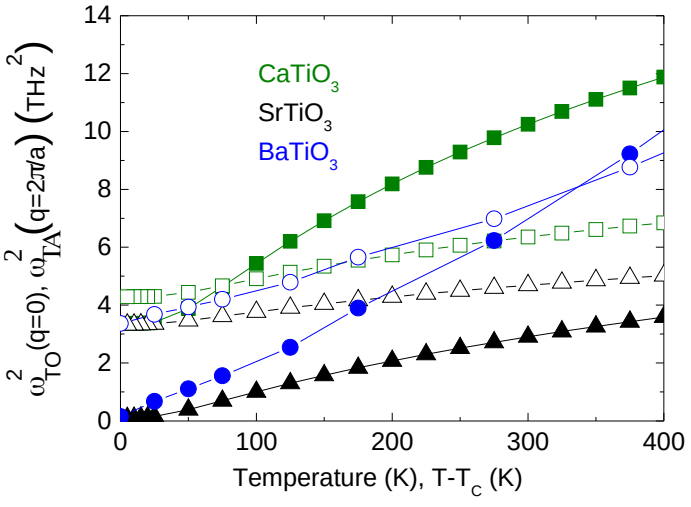

Figure 2 Temperature dependent lowest transverse optic (full symbols) and acoustic modes (open symbols) of CTO (green), STO (black), and BTO (blue). For the latter the temperature is given in terms of (T-T_C)

For the first series the temperature dependent phonon mode dispersions of the lowest TA and TO modes have been presented in Ref. 18. While STO and CTO show dispersions that are very much alike, BTO differs substantially from them since the soft optic mode is almost flat and has Einstein type character at high temperature and smoothly adopts dispersive features with decreasing temperature whereas close to T_C it is similar to what is observed in STO and CTO. Due to the high temperature Einstein-like optical mode behavior, the coupling between optic and acoustic modes in BTO is negligible up to 200K above its phase transition temperature, however for lower temperatures an analogous optic-acoustic mode-mode coupling as in STO and CTO is present. This coupling is evident – as outlined above – in acoustic mode anomalies which are reminiscent of *local soft modes* responsible for intrinsic structural instabilities on finite length scales. In view of the fact that their softening remains incomplete, dynamically distorted elastic and polar nanodomains are a consequence. In addition, a mean free path for phonon-phonon scattering is related to the corresponding scattering vector which has an important impact on the thermal properties of these compounds.

The spatial extension of the polar nanoregions is shown as a function of temperature

for CTO, STO and BTO as a function of T-T_C in Figures 3 (upper figure). As it is obvious from the picture, these exist in all compounds already in the paraelectric phase indicating a local symmetry breaking. With decreasing temperature, respectively, upon approaching T_C in BTO, the nanoregions grow in size and diverge in BTO near T_C as expected for the polar state.

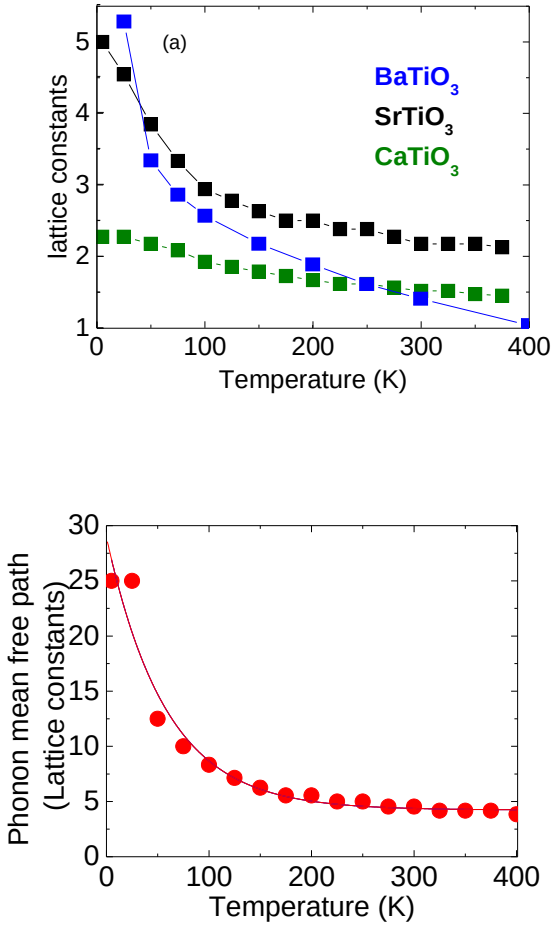

Figure 3 (upper figure) Temperature dependence of the size of polar nanoregions in CTO (green), STO (black), BTO (blue). (lower figure) Phonon mean free path as STO as obtained from the difference in the optic-acoustic mode dispersion.

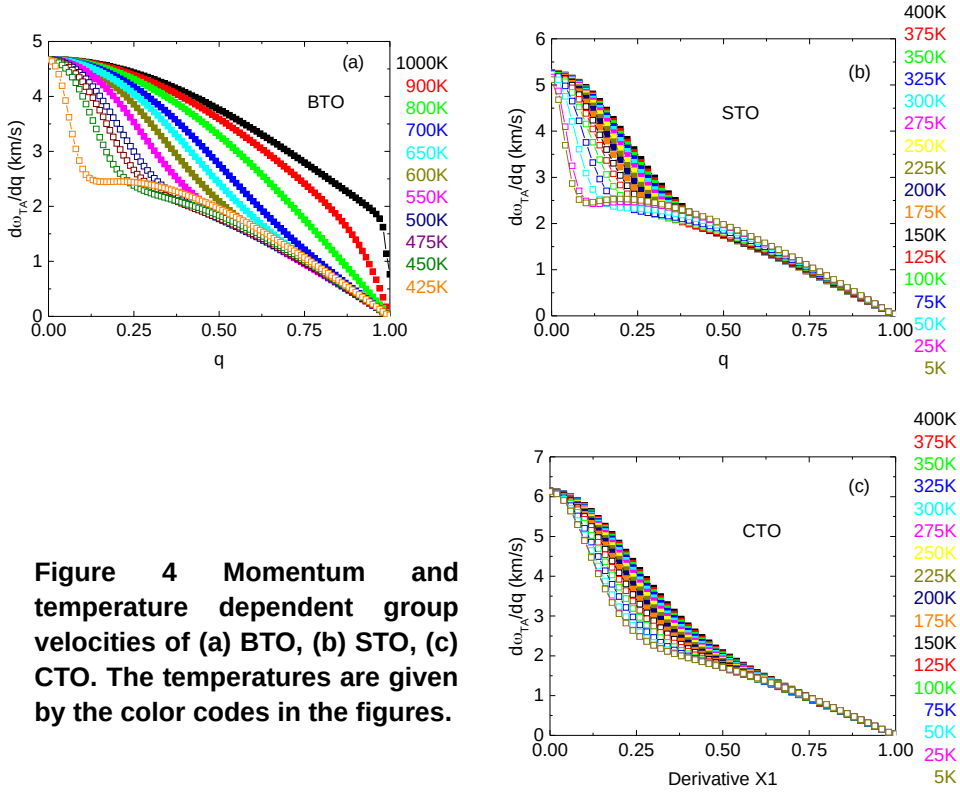

Figure 4 Momentum and temperature dependent group velocities of (a) BTO, (b) STO, (c) CTO. The temperatures are given by the color codes in the figures.

In STO a similar behavior is seen, however, without the divergence in agreement with the suppression of the phase transition whereas in CTO the growth is slow and the length scale remains small, consistent with the fact that its phase transition lies far in the negative temperature region. Yet, in all cases dynamical nanoregions exist in the nominally cubic phase. Their existence has substantial impact on the phonon mode group velocity (Figure 4a – c) which, in turn, massively affects the thermal conductivity, as will be shown as a representative for the case of STO in more detail. As is obvious from Figures 4 the TA mode group velocity of all three compounds becomes anomalous upon approaching T_C in BTO, respectively with decreasing temperature for STO and CTO with STO showing this in a more pronounced way than CTO.

The thermal conductivity (TC) has recently been explored experimentally for STO and doped STO where a novel region in the TC was discovered, namely a regime of phonon Poaiseuille flow where TC evolves faster than cubic in temperature [20]. Basically, the TC is simply the product of specific heat, the phonon mean free path, and the phonon group velocity. All quantities are temperature dependent, which is the

main reason for the difficulties in calculating the TC. Here, however, the Boltzmann transport equation as given below is used:

$$\kappa_{lattice} = \frac{1}{3} \sum_{q,TO,TA} c_v(q)\, v_{q,TO,TA}\, l_{ph}$$

with the c_V being the specific heat and $v_{q,TO,TA}$ the group velocity related to the TO, TA mode and l_{ph} their mean free path which is derived as described above, namely from the phonon-phonon scattering vector as obtained from the phonon mode dispersion difference which is shown for STO in (Figure 3 lower part). Typically this quantity causes the major problem in calculating the TC, since the knowledge of it is difficult to obtain. Very few experimental tools are available from which rather precise information can be obtained. An additional complication lies in the fact that its temperature dependence is hard to estimate and it can vary between a few nm and microns. Since the optic mode contribution is negligible, only the acoustic mode is taken into account. This does, however, not imply that the optic phonons are unimportant, but just the opposite, namely they represent the dominant scattering channel for the heat-carrying acoustic phonons. Omitting these [21–23] would release an enormous increase in the TC. The result for the TC is shown in Figure 5.

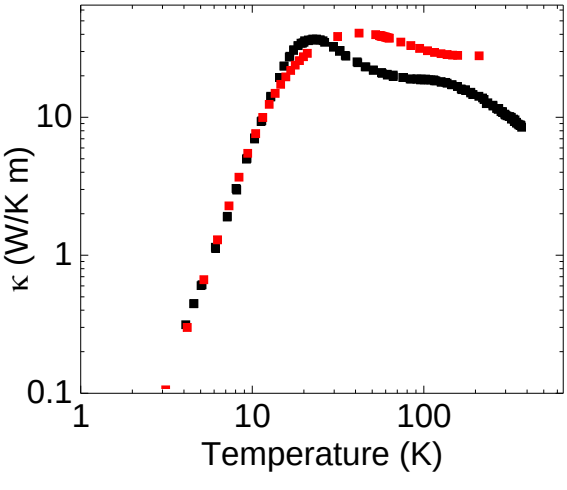

Figure 5 Double logarithmic plot of the temperature dependence of the thermal conductivity of STO. The black points are obtained from experimental data from Ref. 20, the red ones are calculated results.

A comparison with experimental data [20] shows an overall good agreement, even though some experimentally observed fine details are not reproduced, especially for

T>200K where probably further phonon branches need to be taken into account. However, in view the simplicity of this parameter free approach based on the self-consistent phonon theory the overall agreement clearly suggests that anharmonic effects in terms of phonon-phonon interactions which provide the phonon mean free path and the nanoregions length scale, are the basic ingredient to understand the TC of STO and related compounds. It is important to note that the mean free path changes from the order of lattice constants at high temperature to diverging at low temperature and thus provides a natural crossover from kinetic to ballistic transport regimes. The observation of a Poiseuille flow appearing above the Casimir region [20] is attributed to the enhanced quantum fluctuation effects of STO which appear just in this temperature window.

In the second series, rather opposite to the first (Figure 6), the soft zone boundary acoustic phonon modes are unstable prior to the optic mode in PZO and PHO while for PTO the reversed is observed in agreement with the fact that the latter is a “displacive” ferroelectric while the former are antiferroelectric. In PZO and PHO both modes, transverse optic (TO) and transverse acoustic (TA) almost simultaneously soften suggesting the existence of a transient ferroelectric phase / instability [19].

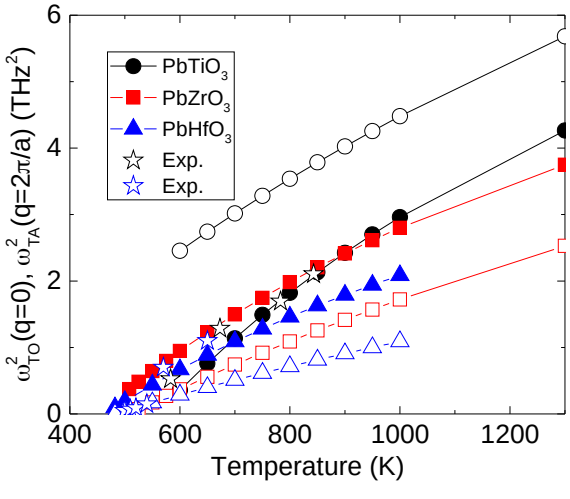

Figure 6 Transverse optic zone center (full symbols) and transverse acoustic zone boundary (open symbols) mode frequencies as a function of temperature for PTO (back), PZO (red), and PHO (blue).

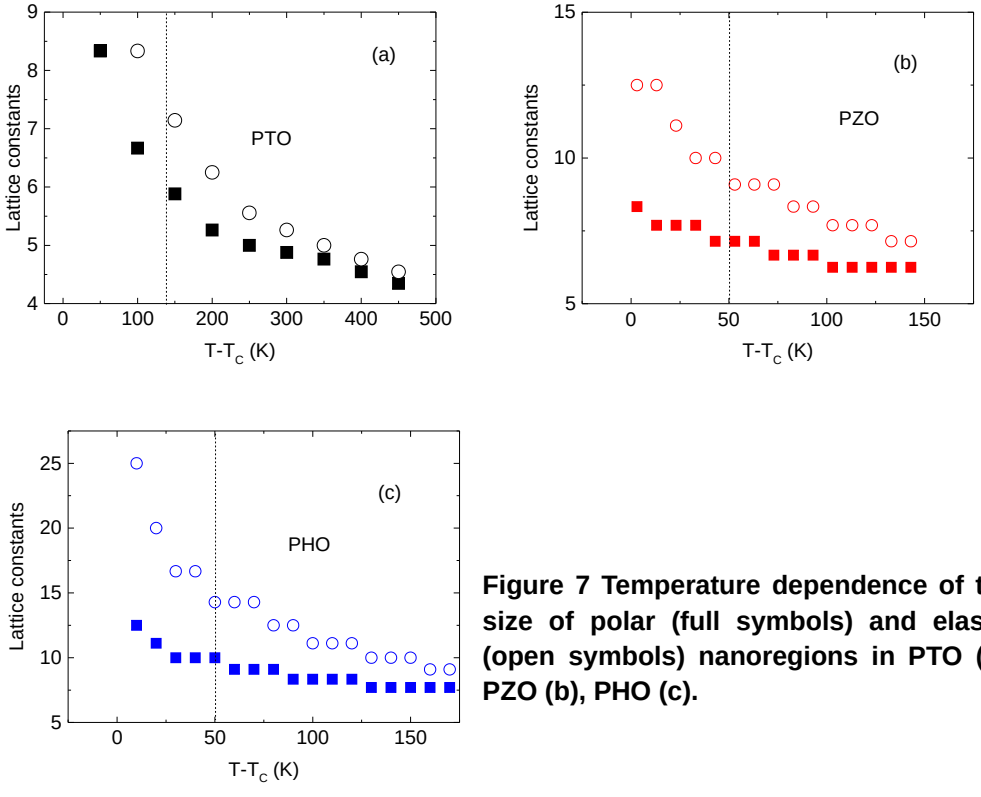

Figure 7 Temperature dependence of the size of polar (full symbols) and elastic (open symbols) nanoregions in PTO (a), PZO (b), PHO (c).

In all three cases, however, a competition between ferro- and antiferroelectric modes is evident, which has led to diverse statements regarding the phase transition mechanisms. While it was claimed that multiple mode softening occur, also incommensurate modulations have been suggested, especially for the case of PZO.

Like in the first series TO-TA phonon-phonon scattering causes anomalies in the acoustic and optic modes where due to the competitive character between optic and acoustic mode softening both, polar and elastic, nanodomains attain importance. The related temperature dependent spatial extents of both domain types are presented in Figures 7. Quite opposite to the previous series the length scales of the nanodomains are much larger and increase from PTO to PZO and to PHO. As already noted in Ref. 19, evidently all three systems show precursor dynamics which are more pronounced for the acoustic mode as compared to the optic one. This fact demonstrates the preference of the system towards an antiferroelectric transition as compared to a polar instability and is the least apparent for PTO. However, these effects appear on different length and temperature scales (even though consistent with the predictions of Ref. 24 where the onset has been determined to take place approximately at $1.1T_C$) which corresponds to ~$(T\text{-}T_C)$=50K for PHO and PZO and to ~$(T\text{-}T_C)$=100K for PTO.

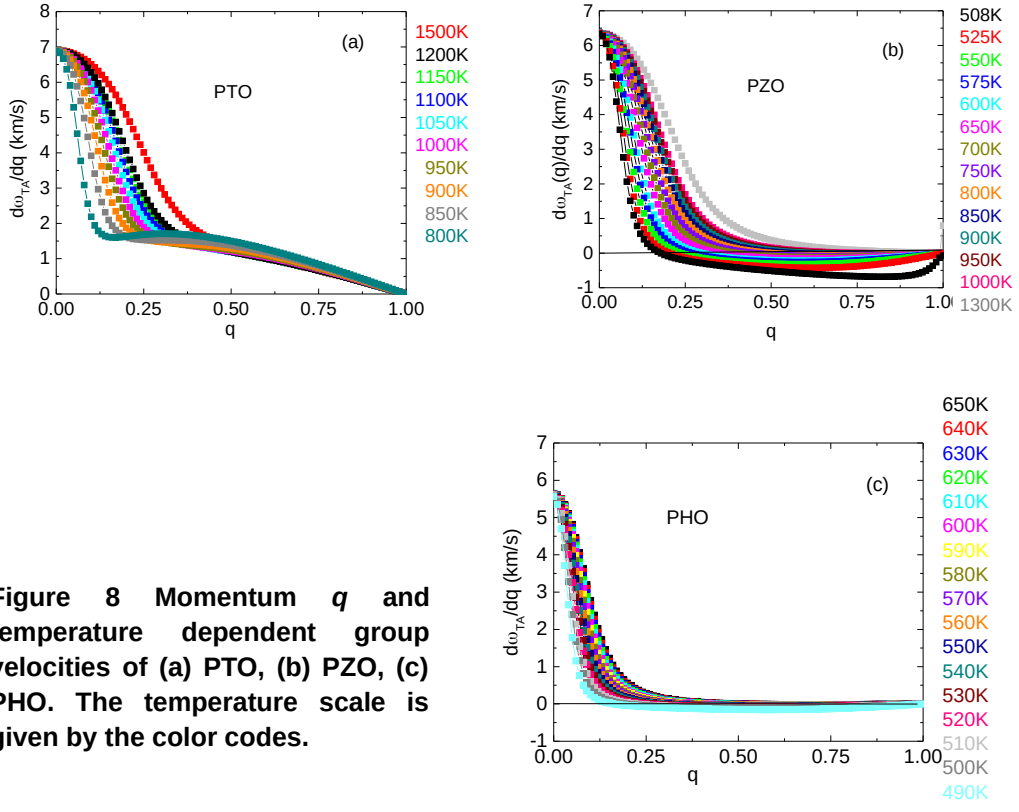

Figure 8 Momentum *q* and temperature dependent group velocities of (a) PTO, (b) PZO, (c) PHO. The temperature scale is given by the color codes.

The spatial extents of the precursor clusters vary largely within the investigated series being very large in PHO to decrease systematically with decreasing transition metal mass (note that the y-axis scale has been changed within Figures. 7). Another obvious difference in the compounds relates to the optic mode related precursor effects (squares in Figs. 7). While these are pronounced and almost of the same order of magnitude as those related to the acoustic mode (open circles in Figs. 6) in PTO, their spatial extent is much reduced in comparison to the acoustic mode related one in PZO and PHO, even though still prominent. This finding is rather remarkable, since PTO has mostly been classified as a prototypical displacive system. However, early on doubts have been raised about this classification in view of distinct order-disorder features [19]. The observation of precursor dynamics is rather inconsistent with the former classification scheme and we conclude that order-disorder effects must be present in this compound as well.

The group velocities of the acoustic modes in this series are shown in Figures 8. While the one of PTO resembles those of STO and CTO, a substantially different behavior is seen in the two remaining systems, where zero or negative group velocities at finite momentum appear.The negative ones correspond to a backward propagation of the acoustic mode group velocity which occurs in a finite spatial region of the sample. Such a negative group velocity value has been predicted in [25–27] and experimentally realized in [28].

The zero group velocity cases correspond to standing waves and are a consequence of broad flat regions in the dispersion as are typical for localized modes or Einstein oscillators. These are more prominent in PHO as compared to PZO and cover a large area in momentum space which is almost temperature independent. The consequences for the thermal conductivities of these three perovskites are that PTO can be placed into the group of BTO, STO and CTO, namely behaving like crystalline solids, whereas PZO and PHO evidence glass like properties. This issue has been debated early on where Lawless [29] adopted the glass like approach for PZO whereas De Yoreo et al [30] favor the crystalline aspect. From the above analysis the glassy behavior is supported since a large range in q-space is covered by localized modes as would be expected for a disordered system.

III. Precursor effects to the phase transitions: Birefringence, dielectric, and strain experiments

In $BaTiO_3$, a variety of techniques have provided evidence for the formation of polar micro-nano-regions well above the cubic–tetragonal phase transition. A kind of convincing proof for pre-transitional effects (locally broken symmetry) is the presence of the birefringence in the paraelectric phase [31], which is forbidden in the centrosymmetric phase (Figure 9). Measurements of birefringence belong to the technique in which the possible influence of measuring factor, as the light intensity here, on physical properties of crystals is reduced to almost zero.

The onset temperature for observing a finite birefringence coincides with the predicted relation $T_{BH} \sim 1.1T_C$ [32] and confirms the important finite momentum mode-mode coupling.

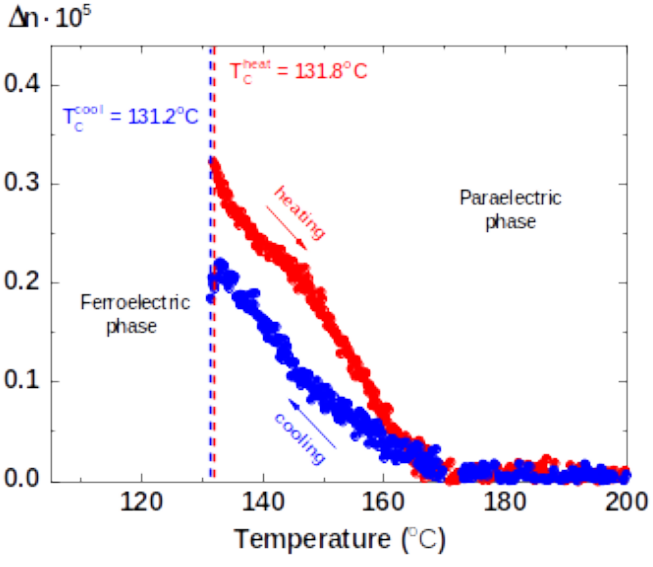

Figure 9. Birefringence measured on cooling (blue circles) and heating (red triangles) for pure $BaTiO_3$ single crystals (after Ref. 31).

The appearance of local polar regions above T_C due to local lattice instabilities can also experimentally be proven by measurements of strain η changes. In every single dielectric there is the electrostrictive effect which is a quadratic function of the applied electric field E, i.e. $\eta=M*E^2$, where M is the field-related electrostrictive coefficient. It appeared that in $BaTiO_3$ single crystals, grown by the top seeded solution growth (TSSG) technique, the measurement of strain above T_C revealed non-classical η(E) dependence. In Figure 10 the temperature dependence of the permittivity close to main phase transition between the cubic and tetragonal phases is presented. For such well-known dependencies for this crystal, the characteristic is the discrepancy of the temperature dependence of the reciprocal permittivity from the Curie-Weiss law in a rather large temperature range above T_C. In fact, the broadness of the region corresponds well to that calculated from the relation $T_{BH}=1.1T_C$ [32]. Assuming that this discrepancy is connected with the existence of polar regions, with their size growing while approaching phase transition point, one can expect changes of the sample sizes as well.

To determine the strain *η* caused by an electric field and related with a polarization *P*

accompanying this action, a method based on the capacitance sensor was used [33,34].

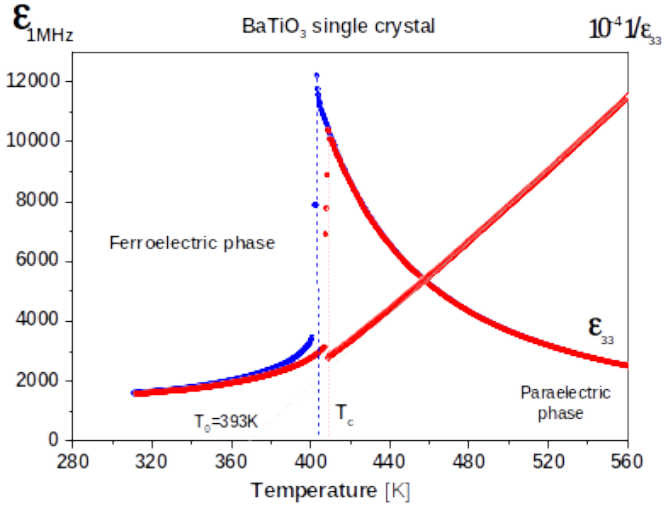

Figure 10. Temperature dependence of the permittivity near the main phase transition point at T_C.

Below 450K clear discrepancies from the Curie-Weiss law (black solid line) are apparent and opposed to experimental data (red open circles) corresponding to the reciprocal values of the permittivity above T_C.

A deformation of the sample was induced by an alternating electric field *E* of frequency 70 Hz and transferred via a quartz rod with one end placed on the sample surface and the second one connected to one of the movable plates of the sensor capacity C_0. The surface of the end of the quartz rod, which touches the crystal, was of the order of 0.02 mm^2. The piezoelectric and electrostrictive deformations could be determined through the registration of the total potential drop U_{total} on a resistance R due to the electric current *i* flowing in the series RC_0 circuit and caused by changes of ΔC of the sensor capacity C_0, and recorded numerically by means of an oscilloscope. The experimental setup has been built based on the scheme shown in Figure 11.

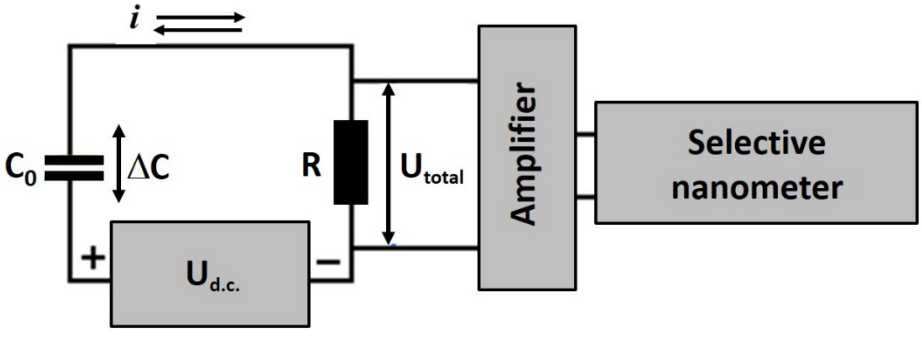

Figure 11. A method of quasi-static strain measurement for a BTO single crystal.

Changes ΔC of the sensor capacity C_0 connected to voltage amplifier of constant value $U_{d.c.}$ cause a current i flowing through the resistance R. To detect the alternating potential drop U_{total} the amplifier was used. Additionally, the selective nanometer made it possible to extract from the U_{total} the piezoelectric and electrostrictive signals separately.

The alternating total potential drop U_{total} is the sum of potential drops $U_{electrostrictive}$ and $U_{piezoelectric}$ generated by the electrostrictive and piezoelectric strains respectively:

$$U_{total} = U_{piezo} + U_{electrostriction} \tag{1}$$

and are described by the following equations:

$$U_{piezoelectric} = \frac{\Delta C_p \omega U R}{\sqrt{1+(RC_0\omega)^2}} \cos(\omega t + \varphi) \qquad \varphi = -R\omega C_0 \tag{2}$$

$$U_{electrostrictive} = \frac{\Delta C_e \omega U R}{\sqrt{1+(RC_0\omega)^2}} \cos(\omega t + \varphi) \qquad \varphi = 2R\omega C_0 \tag{3}$$

where $\omega = 2\pi f$ is the angular frequency with f = 70 Hz, R the resistance, U a constant voltage applied to the condenser C_0, φ is the phase shift between the voltage causing sample vibrations and current *i* causing the potential drop on the resistance R, and ΔC_p and ΔC_e are the amplitudes of changes of the capacity caused by the

electrostrictive and piezoelectric deformations, respectively. It is worth mentioning that the former deformation appears at frequency 2ω, and the latter at ω, and causing time changes of the capacitor C_0 according to the function $C(t) = C_0 + \Delta C_e \sin^2(\omega t)$ and $C(t) = C_0 + \Delta C_p \sin(\omega t)$. Figure 12 presents typical U_{total} signal observed for $BaTiO_3$ single crystal above T_C in <001> direction.

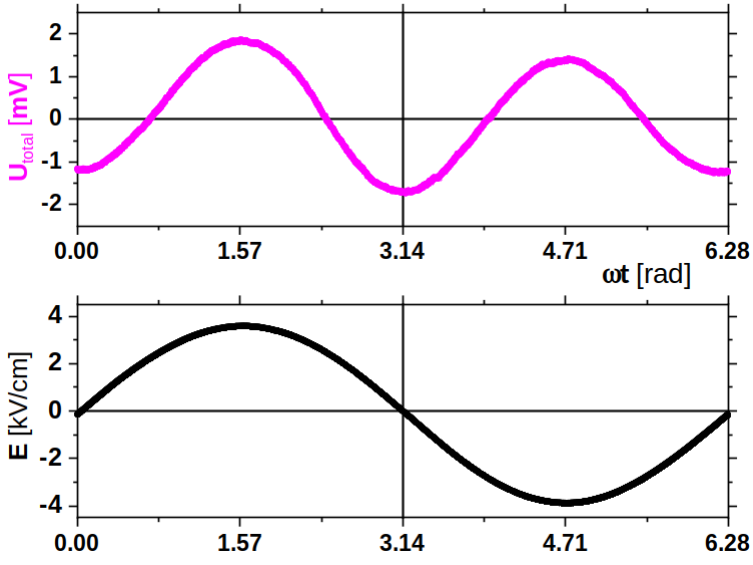

Figure 12. Example of the asymmetrical signal U_{total} detected for $BaTiO_3$ single crystal at 425K, i.e. above T_C.

The origin of this asymmetry is the existence of the piezoelectric deformation which changes in time in accordance with sin(ωt) and adds to the dominating electrostrictive deformation proportional to the $\sin^2(\omega t)$. The lower figure shows the shape of the electric field intensity E applied to the sample. In all experiments the same electric field strength 3kV/cm and frequency 70Hz were used.

For each temperature above T_c the U_{total} detected above T_c was fitted using the function (14) described above. Figure 13 represents an example of such fitting to the U_{total} run shown in the upper part of Figure 12**.**

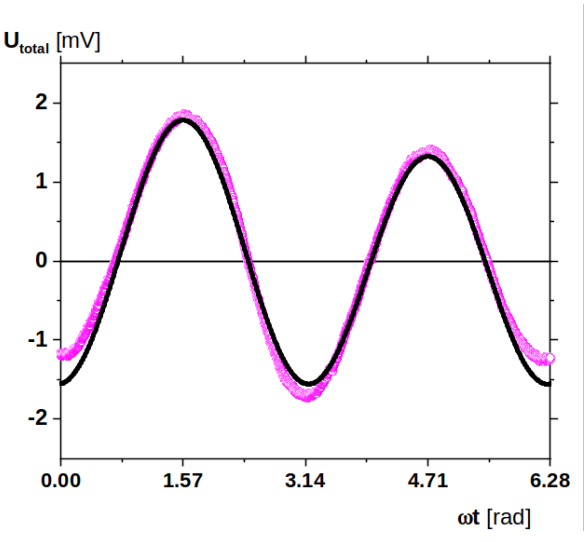

Figure 13. A fit (black curve) to a signal U_{total} detected for $BaTiO_3$ single crystal at 425 K.

From this fit the parameters ΔC_e and ΔC_p are assigned to the values of the electrostrictive and piezoelectric strains.

Having assigned the strains:

$$strain_{piezoelectric} = \frac{\epsilon_0 S}{d_0} \times \frac{\Delta C_p}{C^2_0} = d_{33} E_3 \quad \text{and}$$

$$strain_{electrostrictive} = \frac{\epsilon_0 S}{d_0} \times \frac{\Delta C_\theta}{C^2_0} = M_{33} E^2_3$$

the value and sign of the piezoelectric coefficient d_{33}, and also the value and sign of the field-related electrostrictive coefficient M_{33} can be calculated. Based on these calculations both strain coefficients as a function of the applied electric field E are plotted in Figure 14.

The procedure described above has been used to calculate the piezoelectric and electrostrictive properties of the barium titanate single crystals above the phase transition to the paraelectric phase (i.e. for $T > T_c$). The piezoelectric activity persists in a broad temperature range above T_c, and disappeared above 450 K. This is another confirmation of the theoretically predicted relation $T_{BH} \approx 1.1 T_c$ [32].

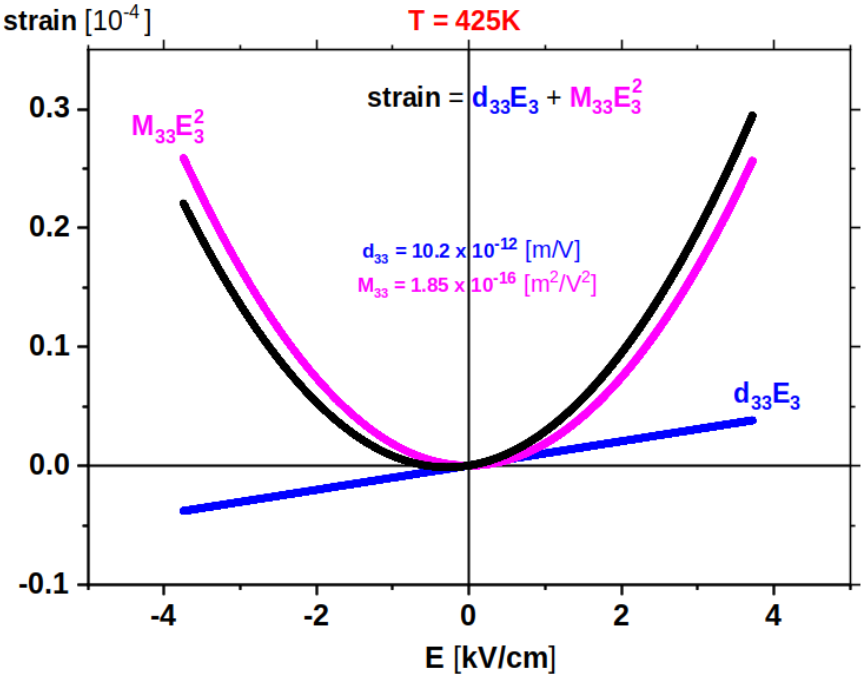

Figure 14. Field dependent strains detected above T_C at 425 K for $BaTiO_3$ single crystal.

Similar, although slightly different, related effects have been found in $PbZrO_3$ and $PbHfO_3$ single crystal with the antiferroelectric phase transitions. Figure 15 shows the permittivity and birefringence as a function of temperature. All these dependences reveal that the paraelectric phase in the sense of Landau theory is developing only above a certain temperature over T_C.

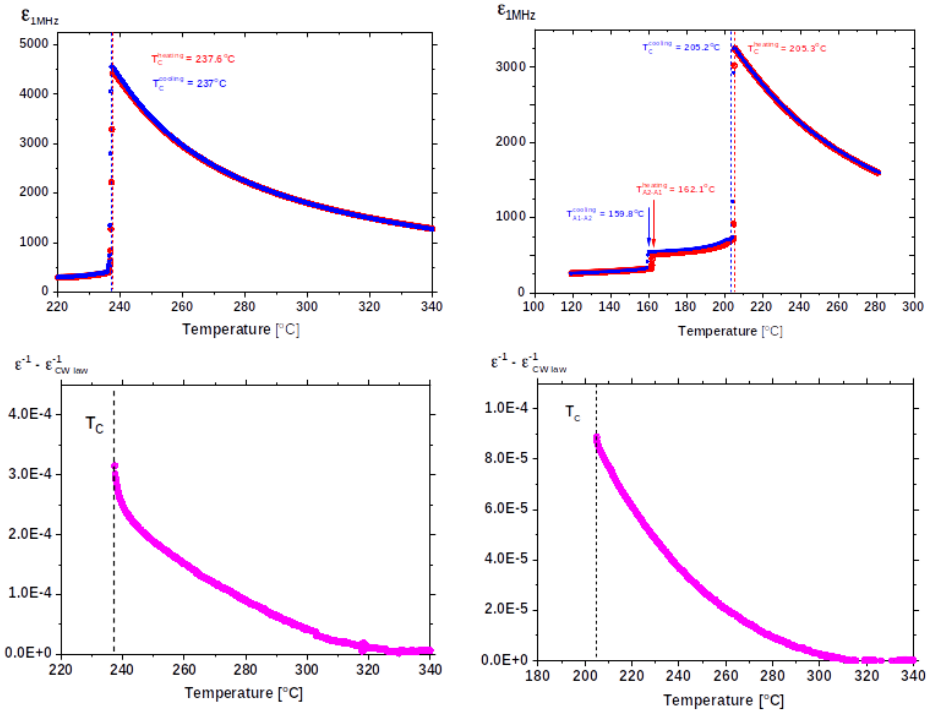

Figure 15. Temperature dependences of the permittivity and its inverse ε, ε^{-1} and birefringence Δn above T_C for single crystal $PbZrO_3$ and $PbHfO_3$.

IV. Precursor effects to the phase transitions: Elastic anomalies of ferroelectric and antiferroelectrics with perovskite structures

Elastic stiffness coefficients (abbreviated as elastic constants hereafter) are one of the fundamental physical properties of solids because they are associated with the interatomic potentials in solids. The measurement of sound velocities and elastic constants has been one of the approaches to studying phase transition behaviors of condensed matters including ferroelectrics [35]. Strains caused by acoustic waves can couple to the order parameter (polarization) of polar dielectrics. In particular, the

electrostrictive coupling between the strain and the squared polarization of precursor polar clusters in ferroelectrics and antiferroelectrics induces anomalous changes in the sound velocities and the elastic constants in the paraelectric phase, which gives us an important chance to look into the pretransitional behaviors of these systems. This part will review the acoustic anomalies of various perovskite-structured ferroelectrics/antiferroelectrics and the implication of these results on the theoretical predictions described above.

Elastic constants can be measured in terms of several experimental methods, such as ultrasonic and Brillouin spectroscopies to name a few. Especially, Brillouin light scattering spectroscopy can be used to probe the long-wavelength acoustic phonon branches near the zone center of the first Brillouin zone. The linear slopes of these phonon branches denote the sound velocities of the LA and the TA modes, from which the elastic constants can be calculated [36]. The wavelength of the acoustic waves probed by Brillouin scattering is usually in the range of 100~300 nm which depends on the scattering geometry. The complete determination of elastic constants of various perovskites over a wide temperature or pressure range has been carried out by several groups. In this section, the acoustic properties of BTO and modified BTO single crystals will be review from the viewpoint of pretransitional behaviors and then those of Pb-based perovskites will follow.

Figure 16(a) shows the temperature dependence of the LA-mode frequency (ν_B) of several kinds of BTO single crystals measured at the backscattering geometry [37-44]. The temperature is rescaled with respect to T_C. The crystal growth methods include top-seeded solution growth (TSSG), flux growth (Flux) and solid-state single crystal growth (SSCG) methods. Figure 16 also includes the data of reduced BTO (R-BTO) and Rh-doped BTO (Rh-BTO). The phonon propagation direction was along the [100] axis in the cubic phase. The ν_B is proportional to the longitudinal sound velocity of the LA mode and related to the elastic constant C_{11}. Figure 16 (b) shows the temperature dependence of the full width at half maximum (FWHM, Γ_B) of the corresponding LA mode. Although the absolute values of Γ_B are different depending on the crystal growth condition and the composition, they exhibit nearly universal behaviors in their paraelectric phases. That is, the LA-mode frequency first increases with decreasing temperature and then begins to show softening upon further cooling. The softening of the mode frequency is accompanied with the increasing FWHM, especially at temperatures close to T_C. It is easily noticed that the temperature range where the changes in the ν_B and the Γ_B are most significant is approximately T_C ~ T_c+(~55) K. The nonzero ν_B is attributed to polarization fluctuations and thus called fluctuations damping [45]. The substantial increase in Γ_B indicates the growth in the size of polar clusters, which is consistent with the theoretical prediction as described.

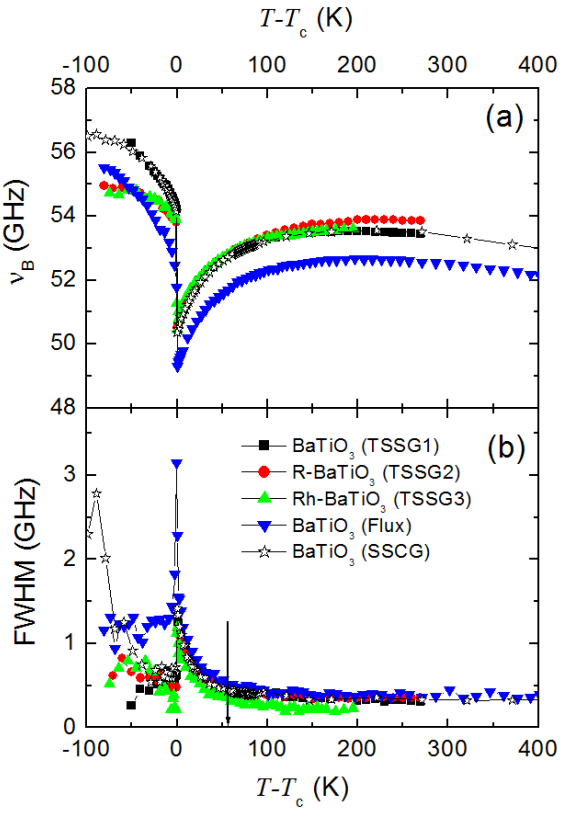

Figure 16. Temperature dependence of (a) ν_B and (b) Γ_B of BTO single crystals grown by using different growth methods.

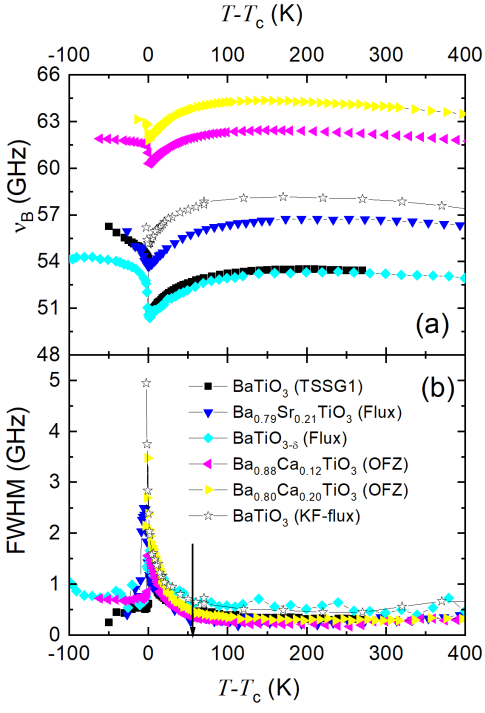

Figure 17. Temperature dependence of (a) ν_B and (b) Γ_B of several BTO single crystals modified with Ca, KF, and oxygen deficient condition.

Figures 17(a) and (b) show temperature dependences of ν_B and Γ_B, respectively, of the LA modes of BTO-based single crystals modified as KF-included BTO(KF-flux), two Ca-substituted BTOs ($Ba_{0.80}Ca_{0.20}TiO_3$ (BCTO-0.20) and $Ba_{0.88}Ca_{0.12}TiO_3$ (BCTO-0.12)), Sr-substituted BTO ($Ba_{0.79}Sr_{0.21}TiO_3$ (BSTO-0.21)) and oxygen-deficient $BaTiO_{3-\delta}$ [36-40]. The two BCTO single crystals were grown by optical floating zone (OFZ) method. All data were measured at the backscattering geometry where the phonon propagation direction was along the cubic [100]. Thus, the associated elastic constant is C_{11}.

Previous studies showed that inclusion of Ca, Sr, K or F into the A or B sites of the perovskite structure introduces substitutional disorder and enhances diffuseness [46-50]. In addition, these substitutions increase the Brillouin shift of the LA mode thus C_{11}. In spite of the difference of C_{11} among these modified single crystals, their acoustic damping behaviors are very similar. The anomalous change in the imaginary part of

the complex elastic constant, Im[ΔC], is related to the squared local polarization P_{local} via the following equation [45], where ω is the angular frequency of the acoustic wave, τ is the relaxation time of the relevant relaxation process, γ is the electrostrictive coupling coefficient between the strain and P_{local}:

$$\mathrm{Im}[\Delta C] = \frac{(\omega\tau)\gamma^2 P^2_{local}}{1+\omega^2\tau^2} \quad \varepsilon \propto P^2_{local}$$

The substantial increase in Γ_B from the constant background damping clearly shows that the size of the precursor polar clusters increases and thus the polarization fluctuations are enhanced below a certain temperature of T_c+(~55) K, which is consistent with the theoretical prediction for the precursor phenomena. This suggestion is further supported by the observation of the formation of quasi-elastic central peaks which represent the relaxational motion of precursor polar clusters.

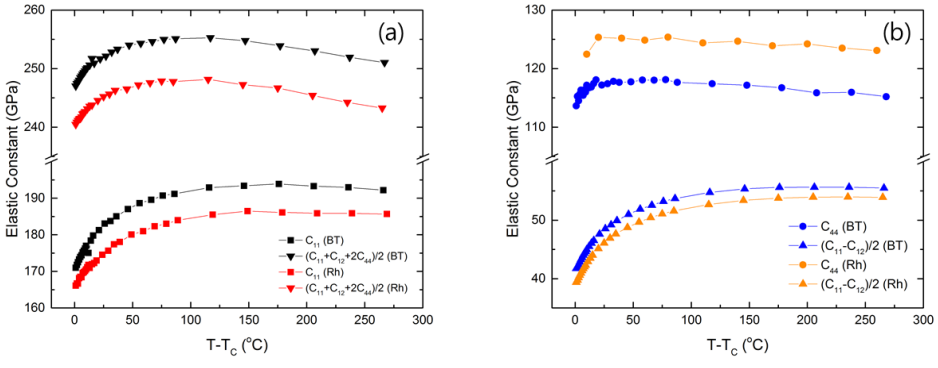

Figure 18. Temperature dependences of the elastic constants of pure BTO(BT) and Rh-doped BTO(Rh) in the paraelectric phase.

Although the systematic investigation of the LA mode of various BTO-based single crystals at the backscattering geometry gives us rich information about the precursor dynamics, it is associated with only one elastic constant C_{11}. Recently, the complete elastic constants of BTO have been reported over a wide temperature range in the paraelectric phase [42-44]. Figure 18 shows the temperature dependences of the elastic constants of pure BTO(BT) and Rh-doped BTO(Rh) in the paraelectric cubic phase. There are three symmetrized eigen elastic constants in the cubic phase [51],

which are tabulated in Table 1. If one of these elastic constants decreases toward zero, the system tends to deform according to the associated symmetry instability. Among them, the C_{44} and $(C_{11} - C_{12})/2$ have attracted attention due to their nature of symmetry instability. C_{44} and $(C_{11} - C_{12})/2$ correspond to the rhombohedral and tetragonal/orthorhombic distortions, respectively. Figure 18 shows that C_{44} is nearly temperature-independent while $(C_{11} - C_{12})/2$ displays a substantial softening at temperatures above T_c. Moreover, the absolute value of $(C_{11} - C_{12})/2$ is much smaller than that of C_{44}. These results clearly indicate that the precursor polar clusters have a local tetragonal symmetry in the paraelectric phase consistent with the result from nuclear magnetic resonance measurements [52, 53]. An even more interesting point about the elastic data is the characteristic temperature below which the $(C_{11} - C_{12})/2$ shows substantial softening, which is approximately T_c+(50-60 K). A similar behavior is also seen from the temperature dependence of C_{11}. These results indicate that the coupling between the polarization of the precursor clusters and the strain caused by acoustic waves becomes stronger in a specific temperature range above T_c, which is again consistent with the theoretical prediction for the stability range of the polar clusters.

Table 1. Relationship between the eigen elastic constants and the structural instability in the cubic phase.

Elastic Constants	$C_{11}+2C_{12}$	$(C_{11} - C_{12})/2$	C_{44}
Structural Instability	Hydrostatic distortion	Tetragonal or orthorhombic distortion	Rhombohedral distortion

Figures 19(a) and (b) show the temperature dependences of the ν_B and the Γ_B, respectively, of the LA modes of PZO and PHO measured at the backscattering geometry [54-58]. The temperature scale is $(T - T_c)$. These two representative antiferroelectrics share some common characteristics, for example, they exhibit intermediate phases between the paraelectric and the low-temperature orthorhombic phases [59]. The elastic data shown in Figure 19 also reveal similar properties between PZO and PHO. The LA-mode frequency shows gradual softening in the paraelectric phase, which becomes more substantial as the temperature decreases toward T_c. This softening process is accompanied by the increase in Γ_B, which exhibits a peak at T_c. The LA mode is split in the intermediate phase between the paraelectric and the antiferroelectric phases in both PZO and PHO. In addition, the appearance of

the TA mode at T_c [54] clearly indicates that the symmetry of the intermediate phase is different from that of the paraelectric phase. This was attributed to the phase coexistence of the high-temperature prototype phase and the low-temperature antiferroelectric phase [54]. The observation of large piezoelectric constant d_{11} or the P-E hysteresis loop suggests that the intermediate phases of PZO and PHO are polar and weak ferroelectric (or ferrielectric) [54, 58]. The theoretical calculation introduced in the first part of this chapter showed that the simultaneous softening of the zone-center TO mode and the zone-boundary TA mode may induce the transient ferroelectric phase below T_c.

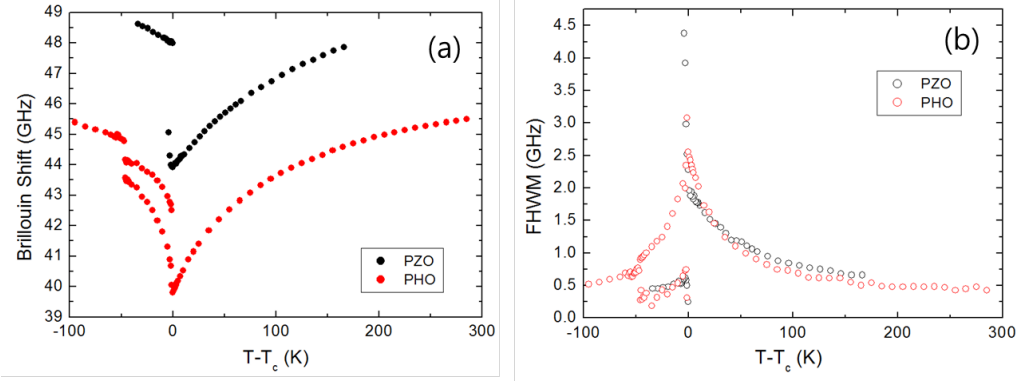

Figure 19. Temperature dependences of (a) the v_B and (b) the Γ_B of the LA modes of PZO and PHO measured at the backscattering geometry.

Temperature dependences of the elastic constants of cubic PZO and PHO single crystals have been reported for the first time by using Brillouin spectroscopy and adopting the forward, symmetric scattering geometry [55, 56, 58]. Figures 20(a)~(d) show the comparisons of the measured elastic constants of PZO and PHO in the paraelectric phase. The elastic constants of PHO should be considered as approximate values due to the slight misalignment of the direction of the phonon propagation direction in the crystal, imperfect parallelism of the two crystal surfaces, etc. [58]. The elastic constants of two antiferroelectrics exhibit very similar behavior, especially the TA mode behaviors in the paraelectric phase. There are two elastic constants corresponding to the two TA modes in the cubic phase, i.e, C_{44} and $(C_{11} - C_{12})/2$. The C_{44} of both PZO and PHO is nearly temperature independent while their $(C_{11} - C_{12})/2$ shows substantial softening in their paraelectric phases. As described above, the C_{44} and $(C_{11} - C_{12})/2$ correspond to the rhombohedral and the

tetragonal/orthorhombic distortions, respectively. The result that only $(C_{11} - C_{12})/2$ becomes softened indicates that precursor clusters of PZO and PHO have tetragonal/orthorhombic distortions in the cubic phase. The acoustic damping represented by the FWHM, as shown in Figure 19(b), also exhibits very similar temperature dependences (i.e. similar magnitude and similar slopes in the temperature window) above T_c. This indicates that the symmetry instability and the corresponding polarization fluctuations in the centrosymmetric cubic phase are similar to each other in PZO and PHO.

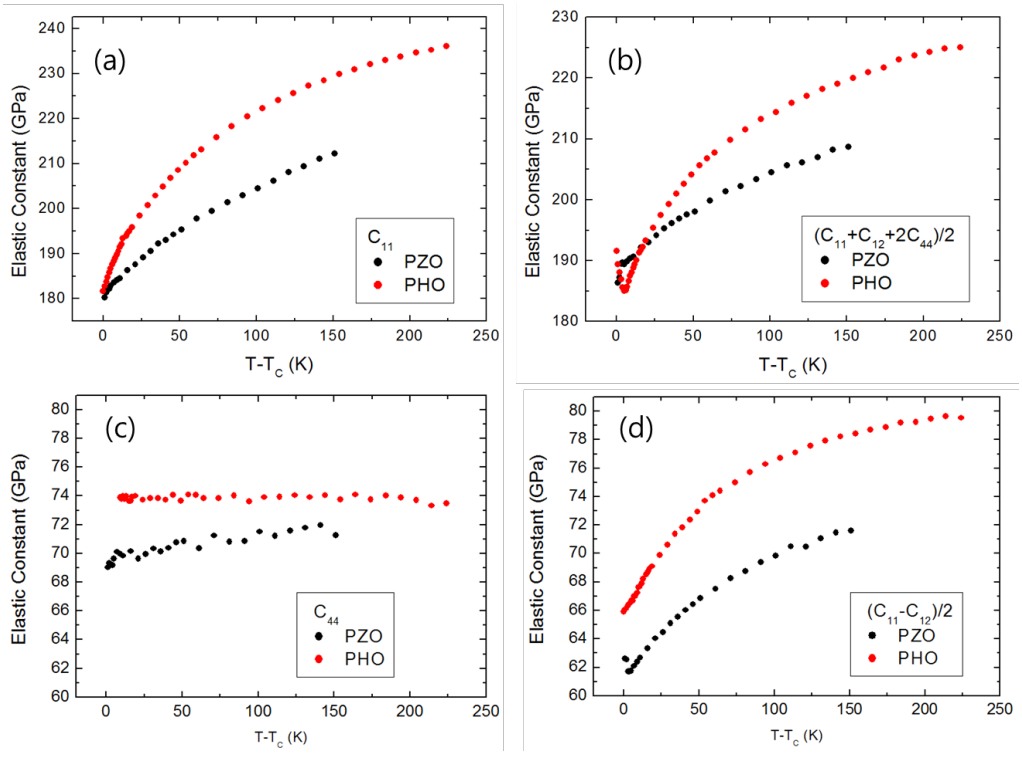

Figure 20. Temperature dependences of the elastic constants of PZO and PHO in their paraelectric phases.

We note that the TA mode behaviors of PZO and PHO are similar to those of BTO shown in Figure 18, i.e., C_{44} was nearly temperature independent and the $(C_{11} - C_{12})/2$ exhibited substantial softening in the paraelectric phase of BTO. One difference is that the magnitudes of C_{44} and $(C_{11} - C_{12})/2$ are similar in both PZO and PHO while C_{44} is much larger than $(C_{11} - C_{12})/2$ in the case of BTO. This difference results in noticeable

difference in the elastic anisotropy parameter A. Zener proposed this parameter A for cubic crystals which was defined as $2C_{44}/(C_{11}-C_{12})$ [60]. A is 1 for isotropic materials and in general larger than unity for normal solids. Figure 21 shows the temperature dependence of A for BTO, PZO and PHO. The parameter A of BTO is larger than 2 and shows a divergent behavior with decreasing temperature toward T_c. On the other hand, although the A's of PZO and PHO gradually increase upon cooling, their values are much smaller than that of BTO and close to unity. This indicates that the orientation-dependent shear moduli in the paraelectric phase of PZO and PHO are similar to those of isotropic materials. As described above, the overall behavior of C_{44} and $(C_{11} - C_{12})/2$ are similar in these three single crystals. The significant difference in A between BTO and PZO/PHO is mainly due to the much smaller $(C_{11} - C_{12})/2$ and much larger C_{44} of BTO compared to those of PZO and PHO. It suggests that BTO is much softer to the tetragonal distortions than the other two crystals, which results in the transition to the tetragonal ferroelectric phase.

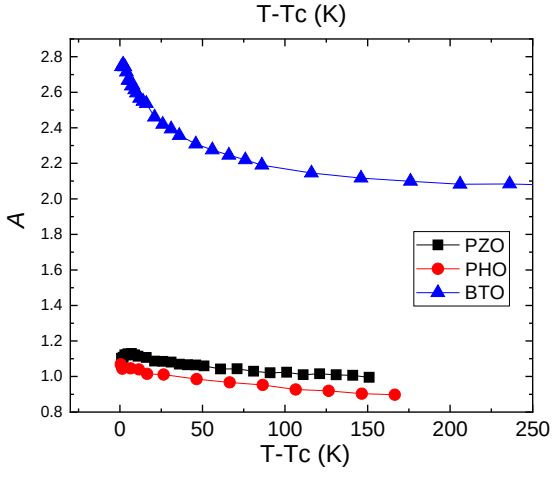

Figure 21. Temperature dependence of *A* for BTO, PZO and PHO.

Substitutional effect of different cations in the perovskite structure has been a powerful method in enhancing various physical properties as well as understanding phase transition behaviors. Effect of Sn substitution in the B-site of PZO and PHO has been investigated systematically. Figure 22 shows temperature dependences of the ν_B and the Γ_B, respectively, of the LA mode of PZO, $PbZr_{0.72}Sn_{0.28}O_3$ (PZSO-0.28) measured at the backscattering geometry [61]. The data of $PbZr_{0.78}Sn_{0.22}O_3$ (PZSO-0.22) were taken from Ref. 62. The LA-mode frequency exhibits noticeable softening in the paraelectric

phase of the three PZO-based single crystals. The acoustic damping is also enhanced upon cooling toward T_c. Especially, the degree of softening of the mode frequency and the maximum of the FWHM become larger with increasing Sn content. In addition, the Sn substitution extends the temperature range of the intermediate phase compared to the pure PZO. PFM (piezoresponse force microscopy) measurements revealed that piezoelectric activity is persistent even in the paraelectric phase of PZSO-0.28 [63] where nonzero birefringence is also observed. These observations clearly indicate the existence of non-centrosymmetric local regions in the centrosymmetric matrix of PZSO.

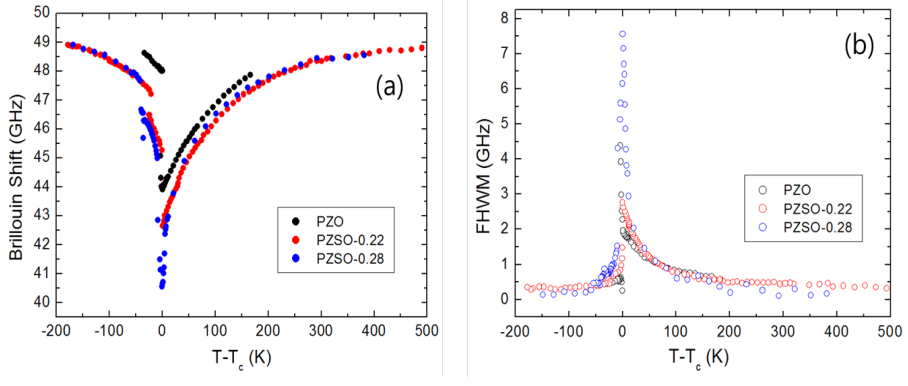

Figure 22. Temperature dependences of (a) ν_B and (b) Γ_B of the LA modes of PZO, PZSO-0.22 and PZSO-0.28 measured at the backscattering geometry. The data of PZSO-0.22 were taken from Ref.62.

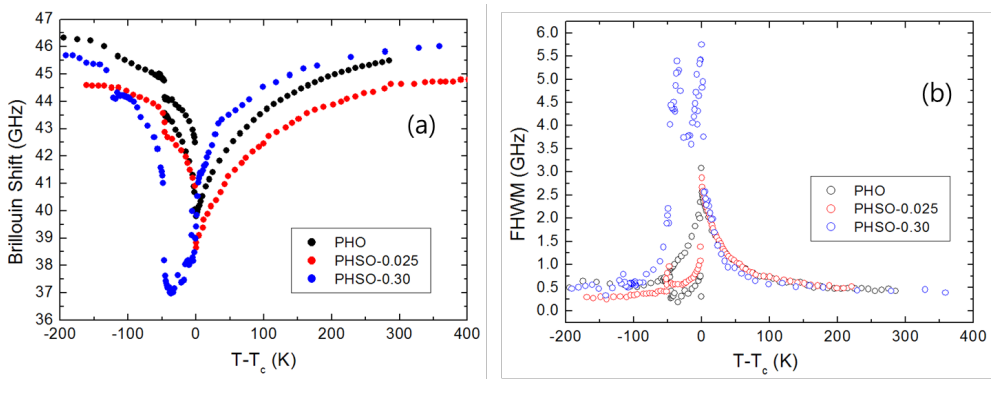

Figure 23. Temperature dependences of (a) ν_B and (b) Γ_B of the LA modes of PHO, PHSO-0.025 and PHSO-0.30 measured at the backscattering geometry. The data of PHSO-0.025 were taken from Ref. 65.

Figure 23 shows temperature dependences of the ν_B and the Γ_B, respectively, of the LA mode of PHO, $PbHf_{0.70}Sn_{0.30}O_3$ (PHSO-0.30) measured at the backscattering geometry [64]. The data of $PbHf_{0.975}Sn_{0.025}O_3$ (PHSO-0.025) were taken from Ref. 65. Similar to the case of PZSO system, PHSO single crystals show mode softening and fluctuations damping in the paraelecric phase. The degree of softening of the mode frequency and the maximum of the acoustic damping become larger with increasing Sn content, which is similar to the case of PZSO. Quasi-elastic central peaks were observed from PHSO, which suggested the slowing-down process of polar clusters as temperature decreased [64]. The Sn substitution makes the intermediate phase very soft, i.e., low frequency mode and very high damping peak are seen in the intermediate phase. This was attributed to the existence of fine ferroelastic domains in the intermediate phase [64, 66].

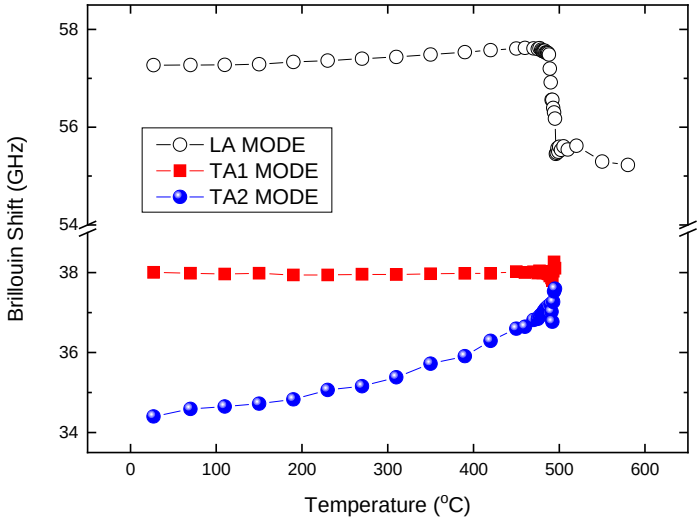

Figure 24. Temperature dependences of ν_B of acoustic modes of PTO measured at the backscattering geometry.

Finally, we briefly review the elastic properties of PTO. Figure 24 shows the temperature dependence of the mode frequencies of three acoustic waves of PTO measured at the backscattering [67, 68]. Only the LA mode is observed in the paraelectric phase of PTO consistent with the Brillouin selection rule [36]. The sudden increase in the LA-mode frequency and appearance of two TA modes at a specific

temperature (~500°C) indicate the ferroelectric phase transition. An interesting point is that the LA-mode frequency is nearly constant in the paraelectric phase. In addition, there is no noticeable central peak component in the light scattering spectrum in the Brillouin frequency window (1~100 GHz). These results are in contrast to other perovskite ferroelectrics and antiferroelectrics which were reviewed above. This difference in the mode behavior may be due to different symmetry property of the central peak and/or different timescales of the relaxation motion of polarization fluctuations [67]. That is, the correlation length of polarization fluctuations of PTO might be very small and the relevant relaxation time may be short compared to other perovskite ferroelectrics and antiferroelectrics. Figure 7 shown in the previous section suggests that the length scale of the nanoregions of PTO is the smallest among PTO, PZO and PHO. The relaxation time of precursor polar clusters of PTO may thus be very short, much shorter than the inverse of the frequency of the acoustic waves resulting in weak or nearly no coupling between the LA mode and the dynamic polar clusters. These results may also be associated with the strong displacive nature of the ferroelectric phase transition of PTO.

All the results reviewed in this section reveal common characteristics of perovskite-type ferroelectrics and antiferroelectrics.

First, the mode frequency of the longitudinal acoustic waves decreases upon cooling in the paraelectric phase except for PTO. This is due to the electrostrictive coupling between the squared local polarization of precursor polar clusters and the strain caused by the LA waves. It is accompanied by the increasing half width which represents the fluctuations damping caused by the local polarizations. The existence of noncentrosymmetric local clusters is further supported by the quasi-elastic central peaks, weak piezoelectric activity and nonzero birefringence in the centrosymmetric cubic phase.

Second, the mode softening and the increase in the acoustic damping become more substantial at temperatures close to T_c. This specific temperature range near T_c is the one where anomalous behavior is observed such as nonzero birefringence and piezoelectric constant, the deviation of the dielectric constant from the Curie-Weiss law, the formation of a strong central peak, etc. It is consistent with the theoretical suggestions based on the nonlinear polarizability model which predicts that the phase transition is preceded by universal precursor dynamics which appear far above T_c. Especially, the theory suggests that the acoustic modes exhibit anomalies close to the long wavelength limit, which develop at high temperatures already above the actual transition temperature.

Third, accurate determination of elastic constants is helpful to our understanding of the symmetry of the structural instability in the paraelectric phase. The TA mode behavior of BTO, PZO and PHO is similar to each other which shows that the C_{44} is nearly

temperature independent while the $(C_{11} - C_{12})/2$ exhibits substantial softening in the paraelectric phase. Considering the Born elastic stability criteria, the anomalous softening of $(C_{11} - C_{12})/2$ indicates that the structural instability caused by the precursor polar clusters is tetragonal and/or orthorhombic in these materials.

Fourth, the LA mode of PTO shows exceptional behavior compared to other perovskites reviewed in this chapter. Nearly temperature-independent behavior of the mode frequency was observed, which may be due to different spatiotemporal behavior of polar clusters and the strongly displacive nature of the phase transition.

V. Conclusion

Perovskite oxides are important for basic research, many technical applications, as substrates, multifunctional tools. Understanding the microscopic properties of this important material class may thus contribute substantially in developing new design strategies to enlarge their technological significance and diversity in device embodiment. In this short review we have chosen to concentrate on their phase transition mechanism which is intimately related to the lattice dynamics. The chosen systems exemplify the diversity of perovskites which varies between ferro-, antiferro-, quantum para-, incipient ferro-, electric states and even possible multiferroic properties in spite of their close relationship. Their commonalities are the cubic structure at high temperature and strong phonon mode softening either related to the Γ or R point in the Brillouin zone. These soft phonon modes have been shown to deviate in their temperature behavior from predictions of Landau theory and rigid ion models according to which they should follow the law:

$$\omega^2(T) \approx (T - T_C)^{\gamma}, \quad \gamma = 1$$

Instead, much more complex characteristics are observed where γ changes from 2 in the quantum limit via 1 in the mean-field regime to 1/3 in the saturation region, with intermediate values between these main zones. These alterations in γ are successfully reproduced by the polarizability model where the peculiar properties of the oxygen ion O^{2-} are incorporated, namely a volume, temperature and pressure dependent anisotropic polarizability. The latter is accounted for introducing an anisotropic nonlinear core-shell coupling constant which induces complex temperature dependent renormalizations of the soft mode, the dielectric permittivity, and

the ferroelectric properties in agreement with experimental data. Importantly, the strong nonlinearity and anharmonicity provide mode – mode coupling at finite momentum which bears reference to finite size domain formation and pre-transitional anomalies and thus definitely rules out the existence of either purely displacive or purely order/disorder transitions. Instead, the predictions from the modelling demonstrate that always a coexistence of both dynamics is realized with the one or the other being dominant. The precursor effects just trace this coexistence since local dynamics are embedded in long wave length solutions. Furthermore, we have chosen two series of perovskites, namely, one where the A-site sublattice ion is exchanged and B remains the same, and a second where the B-site sublattice is replaced but A stays the same. Surprisingly, the rigid A ion sublattice has a much greater effect on the lattice dynamics and the ground state properties of the corresponding compound than anticipated. Its mass, size, polarizability, and spin state massively influence the phase transitions and possible further characteristics. Thus, in the investigated perovskites quantum paraelectricity and incipient ferroelectricity are observed as well as displacive type ferroelectric ground states and order / disorder like polar states. The case of $EuTiO_3$ is special since the Eu $4f^7$ electronic configuration admits for antiferromagnetic order at low temperature in addition to a very complex phase diagram. Upon exchanging the transition metal ion at the B site, the polar order changes to antiferroelectric and simply the mass plays the dominant role.

Even though all investigated perovskite oxides exhibit quite diverse properties, a common feature is their mode softening and the pre-transitional dynamics, which characterize these materials and have been both successfully modelled and experimentally verified.

Cite this paper: A. Bussmann-Holder, J-H. Ko, K. Roleder, OAJ materials and Devices, vol 5(1) chap No3 in “Perovskites and other Framework Structure Crystalline Materials”, p103 (Coll. Acad. 2021) - DOI:10.23647/ca.md20202805

REFERENCES

1. M. E. Lines and A. M. Glass, Principles and applications of ferroelectrics and related materials, Clarendon Press, Oxford, 1977
2. G. Völkel and K. A. Müller, Phys. Rev. B **76**, 094105 (2007)
3. G. Burns, and F. Dacol, Physical Review B. **28**, 2527 (1983)
4. For recent reviews on relaxors see e.g. R. A. Cowley , S. N. Gvasaliya , S. G. Lushnikov, B. Roessli, and G. M. Rotaru, "Relaxing with relaxors: a review of relaxor ferroelectrics", Advances in Physics, 60:2 229-327, (2011); L. Eric Cross, Relaxor ferroelectrics, Ferroelectrics **76**, 241-267 (1987)
5. H. Thomas, IEEE Trans. Magn. **5**, 847 (1969); H. Thomas, Structural Phase Transitions and Soft Modes ed. E. J. Samuelsen (Oslo: Universitetsvorleiget) p. 15 (1971)
6. R. Blinc and B. Žekš, Dynamics of order-disorder-type ferroelectrics and anti-ferroelectrics, Advances in Physics **21**, 93 (1972)
7. R. E. Cohen and H. Krakauer, Phys. Rev. B **42**, 6416 (1990)
8. R. E. Cohen and H. Krakauer, Ferroelectrics **136**, 65 (1992)
9. R. D. King-Smith and D. Vanderbilt, Phys. Rev. B **49**, 5828 (1994)
10. S. Tinte and M.G. Stachiotti, Phys. Rev. B **58**, 11959 (1998)
11. R. Migoni, H. Bilz, and D. Bäuerle, Phys. Rev. Lett. **37**, 1155 (1976)
12. R. A. Cowley, Advances in Phys. **10**, 401 (1960)
13. G. Benedek, A. Bussmann-Holder, and H. Bilz, Phys. Rev. B **36**, 630 (1987)
14. A. Bussmann-Holder and A. R. Bishop, Phys. Rev. B **70**, 184303 (2004)
15. J. C. Slonczewski and H. Thomas, Phys. Rev. B **1**, 3599 (1970)
16. E. Pytte and J. Feder, Physical Review **187**, 1077 (1969)
17. A. Bussmann-Holder, J. Phys.: Condens. Matter **24**, 273202 (2012)

18. A. Bussmann-Holder, K. Roleder, and Jae-Hyeon Ko, J. Phys. Chem. Solids **117**, 148 (2018)
19. For references and more details see e.g. A. Bussmann-Holder, K. Roleder, and Jae-Hyeon Ko, J. Phys.: Condens. Matter **26**, 275402 (2014)
20. Valentina Martelli, Jimenez Julio Larrea, Mucio Continentino, Elisa Baggio-Saitovitch, and Kamran Behnia, Phys. Rev. Lett. **120**, 125901 (2018)
21. M. Omini and A. Sparavigna, Phys. Rev. B **53**, 9064 (1996)
22. M. Omini and A. Sparavigna, Nuovo Cimento D **19**, 1537 (1997)
23. D. A. Broido, A. Ward, and N. Mingo, Phys. Rev. B **72**, 014308 (2005)
24. A. Bussmann-Holder, H. Beige, and G. Völkel, Phys. Rev. B **79**, 184111 (2009)
25. R. Y. Chiao, Phys. Rev. A **48**, R34 (1993)
26. M. Ware, S. A. Glasgow, and J. Peatross, Opt. Express **9**, 506 (2001)
27. M. Ware, S. A. Glasgow, and J. Peatross, Opt. Express **9**, 519 (2001)
28. George M. Gehring, Aaron Schweinsberg, Christopher Barsi, Natalie Kostinski, Robert W. Boyd, Science **312**, 895 (2006)
29. W. N. Lawless, Phys. Rev. B **30**, 6555 (1984)
30. Hanyin Cui, Weijun Lin, Hailan Zhang, and Xiuming Wang, J. Acoust. Soc. Am. **135**, 3398 (2014)
31. A. Ziębińska, D. Rytz, K. Szot, M. Górny, and K. Roleder, J. Phys.: Condens. Matter 20, 142202 (2008).
32. A. Bussmann-Holder, H. Beige, and G. Völkel, Phys. Rev. B **79**, 184111 (2009).
33. M. E. Caspari and W. J. Merz, The electromechanical behavior of BaTiO3 single-domain crystals. Phys. Rev. **80**, 1082 (1950).
34. K. Roleder, Measurement of the high-temperature electrostrictive properties of ferroelectrics. J. Phys. E: Sci. Instrument **16**, 1157–1159 (1983).
35. H. Z. Cummins and A. P. Levanyuk, Light Scattering near Phase Transitions, North-Holland, Publishing Co., Amsterdam, 1983.

36. R. Vacher and L. Boyer, Phys. Rev. B **6**, 639 (1972).

37. J. -H. Ko, S. Kojima, T. -Y. Koo, J. H. Jung, C. J. Won and N. J. Hur, Appl. Phys. Lett. **93**, 102905 (2008).

38. J. -H. Ko, T. H. Kim, K. Roleder, D. Rytz and S. Kojima, Phys. Rev. B **84**, 094123 (2011).

39. J. -H. Ko, T. H. Kim, S. Kojima, K. Roleder and D. Rytz, Phase Transit. **85**, 718 (2012).

40. J.–H. Ko, T. H. Kim, S. Kojima, K. Roleder, D. Rytz, C. J. Won, N. J. Hur, J. H. Jung, T.-Y. Koo, S. B. Kim and K. Park, Curr. Appl. Phys. **12**, 1185 (2012).

41. S. H. Oh, J.-H. Ko, H.-Y. Lee, I. Lazar and K. Roleder, Molecules **23**, 3171 (2018).

42. J. W. Lee, J.-H. Ko, K. Roleder and D. Rytz, Appl. Phys. Lett. **114**, 072901 (2019).

43. J. W. Lee, J.-H. Ko, K. Roleder and D. Rytz, J. Korean Phys. Soc. **74**, 1089 (2019).

44. J. W. Lee, J.-H. Ko, K. Roleder and D. Rytz, J. Korean Phys. Soc. **75**, 404 (2019).

45. W. Rehwald, Adv. Phys. **22**, 721 (1973).

46. J.-H. Ko, S. Shin, M. Jang, C. J. Won and N. Hur, Curr. Appl. Phys. **18**, 44 (2018).

47. T. H. Kim, S. Kojima, K. Park, S. B. Kim and J.-H. Ko, J. Phys.: Condens. Matter. **22**, 225904 (2010).

48. T. H. Kim, J.-H. Ko, S. B. Kim, K. Park and S. Kojima, Ceram. Int. **38S**, S21 (2012).

49. T. H. Kim, J.-H. Ko, S. B. Kim, K. Park, and S. Kojima, Ceram. Int. **38S**, S21 (2012).

50. S. Shin, J.-H. Ko, C. J. Won, and N. Hur, J. Korean Phys. Soc. **66**, 989 (2015).

51. R. A. Cowley, Phys. Rev. B **13**, 4877 (1976).

52. B. Zalar, V. V. Laguta and R. Blinc, Phys. Rev. Lett. **90**, 037601 (2003).

53. B. Zalar, A. Lebar, J. Seliger, R. Blinc, V. V. Laguta and M. Itoh, Phys. Rev. B**71**, 064107 (2005).

54. J.-H. Ko, M. Górny, A. Majchrowski, K. Roleder and A. Bussmann-Holder, Phys. Rev. B **87**, 184110 (2013).

55. A. K. Tagantsev, K. Vaideeswaran, S. B. Vakhrushev, A. V. Filimonov, R. G. Burkovsky, A. Shaganov, D.Andronikova, A. I. Rudskoy, A.Q.R Baron, H.Uchiyama, D. Chernyshov, A. Bosak, Z. Ujma, K. Roleder, A. Majchrowski, J.-H. Ko and N. Setter, Nat. Commun. **4**, 2229 (2013).

56. R. G. Burkovsky, A. K. Tagantsev, K. Vaideeswaran and N. Setter, S. B. Vakhrushev, A. V. Filimonov, A. Shaganov, D. Andronikova, and A. I. Rudskoy, A. Q. R. Baron, H. Uchiyama, D. Chernyshov, Z. Ujma and K. Roleder, A. Majchrowski and J.-H. Ko, Phys. Rev. B **90**, 144301 (2014).

57. J.-H. Ko, K. Roleder, A. Majchrowski and A. Bussmann-Holder, J. Korean Phys. Soc. **64**, 1169 (2014).

58. A. Bussmann-Holder, T. H. Kim, B. W. Lee, J.-H. Ko, A. Majchrowski and K. Roleder, J. Phys.: Condens. Matter. **27**, 105901 (2015).

59. D. L. Corker, A. M. Glazer, J. Dec, K. Roleder and R. W. Whatmore, Acta Cryst. B**53**, 135 (1997).

60. C. Zener, Elasticity and Anelasticity of Metals, University of Chicago, Chicago, 1948.

61. J.-H. Ko, M.-S. Jeong, B. W. Lee, T. H. Kim, I. Jankowska-Sumara, A. Majchrowski, A. Bussmann-Holder, Y. H. Ko, K. J. Kim, A. Soszyński and K. Roleder, Ferroelectrics **479**, 1 (2015).

62. M. Mączka, T.H. Kim, M. Ptak, I. Jankowska-Sumara, A. Majchrowski and S. Kojima, J. Alloys Comp. **587**, 273 (2014).

63. Jankowska-Sumara, Phase Transit. **87**, 685 (2014).

64. J.-T. Hong, B. W. Lee, J.-H. Ko, I. Jankowska-Sumara, M. Podgórna and A. Majchrowski, Curr. Appl. Phys. **18**, 642 (2018).

65. M. Ma˛czka, T. H. Kim, A. Ga˛gor, I. Jankowska-Sumara, A. Majchrowski and S. Kojima, J. Alloys Comp. **622**, 935 (2015).

66. I. Jankowska-Sumara, J.-H. Ko, M. Podgórna, S. H. Oh and A. Majchrowski , J. Appl. Phys. **122**, 104104 (2017).

67. J.-H. Ko, T. H. Kim, S. Tsukada, S. Kojima, and Tae-Yeong Koo, Ferroelectrics **420**, 66 (2011).

68. S. Shin, J.-H. Ko, S. Tsukada, Y. Akishige, K. Roleder and D. Rytz, J. Adv. Dielectr. **5**, 1550011 (2015)